

*Chapter 5***MORPHOLOGICAL EXPRESSION OF THE COHERENCE AND
RELATIVE PHASE OF OPTICAL INPUTS TO THE
PHOTOELECTRODEPOSITION OF NANOPATTERNED SE-TE
FILMS**

Carim, A. I.; Batara, N. A.; Premkumar A.; May, R.; Atwater, H. A.; Lewis, N. S. *Nano Letters*, **2016**, *16*, 2963-2968. DOI: 10.1021/acs.nanolett.5b04999

5.1 Introduction

In this chapter, the morphologies of Se-Te photoelectrodeposits generated using two same-wavelength illumination sources were investigated with a series of discrete linear polarizations in tandem, either both mutually incoherent or mutually coherent with defined phase differences. In conjunction with the experiments, the morphologies of the resulting deposits were simulated by computational modeling of the light-material interactions intrinsic to the photoelectrochemical growth process. This collective assessment examines the capacity of the deposition process to generate unique morphologies in response to discrete net polarization states, and thus to display sensitivity toward the coherency, phase difference, and polarization orientations of the optical inputs. Such further elaboration of the relationship between the illumination and resultant morphology enables the use of deliberately tailored excitation to tune the programmable growth of the deposited material.

5.2 Results and Discussion

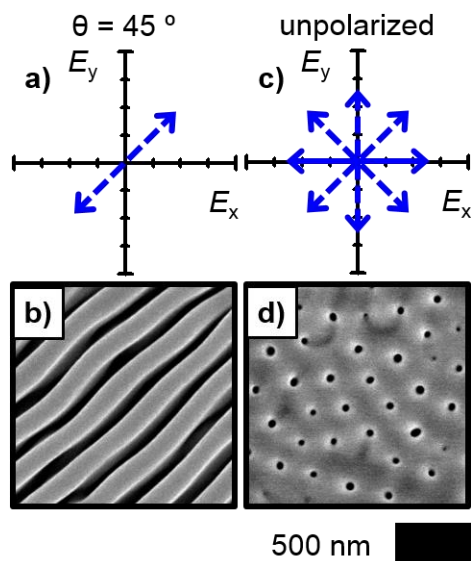


Figure 5.1. Effect of illumination source polarization on anisotropy and orientation of photoelectrodeposit morphology. (a) Plot of the E-field vector of a LED source with $\lambda_{\text{avg}} = 630$ nm linearly polarized 45° clockwise from the vertical, and (b) SEM representative of a photoelectrodeposit generated with this source. (c) Plot illustrative of the many E-field vectors characteristic of the same source as in (a) when unpolarized, and (d) SEM representative of a photoelectrodeposit generated with such source in the unpolarized state.

Se-Te photoelectrodeposits were generated using illumination from a single LED source with $\lambda_{\text{avg}} = 630$ nm and which was linearly polarized such that the E-field component was oriented at an angle $\theta = 45^\circ$ clockwise from the vertical as indicated in the plot presented in Figure 5.1(a). Figure 5.1(b) presents a representative SEM of the deposit morphology which reveals a highly anisotropic lamellar-type morphology wherein the long axes of the lamellae are oriented parallel to the direction of the E-field during growth.^{47,58,59} Quantitatively, the long axes of the lamellae were oriented at $45 \pm 3^\circ$ clockwise from the vertical (θ_{obs}). Deposits were also generated in the same

manner as in (b), but without the use of any polarizing optic, so that the illumination was unpolarized as indicated in the plot presented in Figure 5.1(c), and a representative SEM is presented in Figure 5.1(d). The use of unpolarized light resulted in the generation of an ordered, isotropic mesh-type morphology that consisted of an array of nanopores. Thus, both linearly polarized and unpolarized illumination effect material patterning, but the asymmetry inherent in the linearly polarized illumination creates morphological anisotropy and directs the orientation of the lamellae in the photoelectrodeposit.

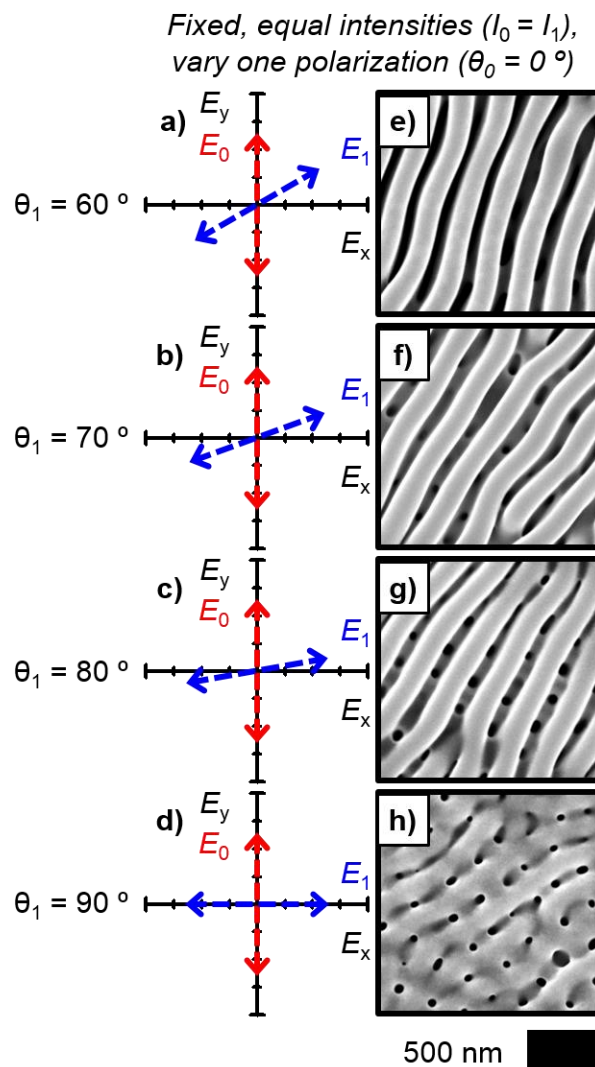


Figure 5.2. Two-source illumination polarization effect on photoelectrodeposit morphology for near-orthogonal and orthogonal polarizations. (a)-(d) Plots of the E-field vectors, E_0 and E_1 , of two incoherent LED sources with $\lambda_{\text{avg}} = 630$ nm and equal intensity, the first source polarized vertically ($\theta_0 = 0^\circ$) and the second at the indicated rotation (θ_1) clockwise from the vertical, and (e)-(h) SEMs representative of photoelectrodeposits generated using these sources.

Subsequent deposits were generated by simultaneously using two incoherent LED sources that had $\lambda_{\text{avg}} = 630$ nm and equal intensities, with the first source polarized vertically ($\theta_0 = 0^\circ$) and the second source offset clockwise from the vertical

by $\theta_1 = 60^\circ, 70^\circ, 80^\circ,$ or 90° . The E-field vectors of each of the two tandem sources are plotted for each condition in Figure 5.2(a)-(d). SEMs representative of the resultant deposit morphologies are presented in Figure 5.2(e)-(h). With $\theta_1 = 60^\circ$, a lamellar-type morphology, similar to that generated with a single illumination source, was observed (Figure 5.2(e)), with a value of $\theta_{\text{obs}} = 27 \pm 4^\circ$. This value agrees with the intensity-weighted average polarization orientation, $0.5 \cdot \theta_1$ for the conditions here, or specifically 30° for the case of $\theta_1 = 60^\circ$, and is consistent with behavior observed previously for $0^\circ < \theta_1 < 60^\circ$.⁵⁹ Such agreement suggests that essentially identical morphologies should be generated using either a single linearly polarized source with orientation θ , or two linearly polarized sources having an average polarization orientation θ . However, when the difference between the polarization orientations of the sources increased past $\theta_1 \approx 60^\circ$, the morphologies observed for the use of two same-wavelength (630 nm) sources with equal intensities, but differing linear polarizations, were more complex than simple lamellar patterns (Figure 5.2(f)-(h)). Beyond this limit, oriented lamellae were still observed, and, for $\theta_1 = 70^\circ, 80^\circ,$ and 90° , $\theta_{\text{obs}} = 32 \pm 6^\circ, 38 \pm 5^\circ,$ and $46 \pm 8^\circ$, respectively. The behavior is thus consistent with expectations based on the average polarization orientation. However, as θ_1 was increased, a mesh-type pattern at a height lower than the diagonal-running lamellae also became apparent (Figure 5.2(f)-(h)), and when $\theta_1 = 90^\circ$ (Figure 5.2(h)) the height of this pattern approached the height of the lamellae. The morphology observed when $\theta_1 = 90^\circ$ (Figure 5.2(h)) was not identical to that generated with a single source oriented at $\theta = 45^\circ$ (Figure 5.1(b)), but rather exhibited significantly less-defined

anisotropy, resembling an average of the morphologies observed for the single source oriented at $\theta = 45^\circ$ and for the unpolarized source (Figure 5.1(d)).

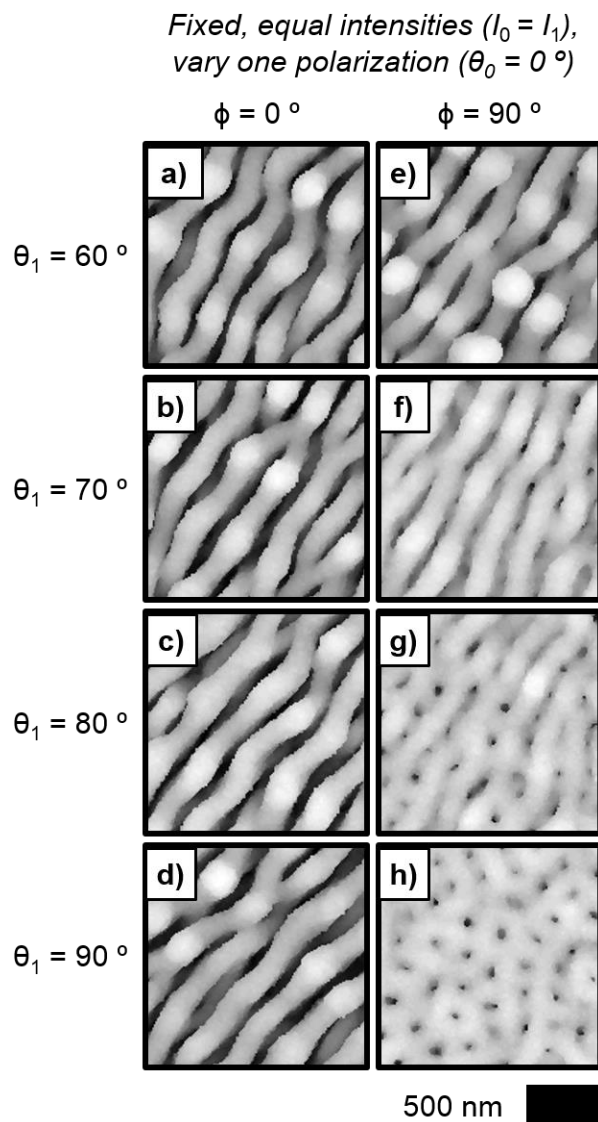


Figure 5.1. Simulated photoelectrodeposit morphologies generated using two fully in-phase or fully out-of-phase coherent, same-wavelength sources with equal intensities and near-orthogonal or orthogonal polarizations. $\lambda = 630$ nm for both sources. The first source is polarized vertically ($\theta_0 = 0^\circ$) and the second at the indicated rotation (θ_1) clockwise from the vertical. Simulations are presented under two conditions: one with a phase angle between the two coherent sources of $\phi = 0^\circ$ (fully in-phase) (a)-(d), and with $\phi = 90^\circ$ (fully out-of-phase) (e)-(h). In both (a)-(d) and (e)-(h) the E-field vectors of the two sources are as indicated in Figure 2(a)-(d), respectively.

The appearance of the mesh-like component of the morphology, and the associated reduction of the uniaxial anisotropy, is consistent with the incoherent nature of the illumination sources utilized in these experiments. Computer modeling of the photoelectrochemical growth process was consequently performed to simulate the morphologies expected for films generated using simultaneous illumination with two coherent sources. The two-step, iterative model described in Chapter 1 was utilized wherein electromagnetic simulations were first used to calculate the local photocarrier-generation rates at the electrode/solution interface and then electrochemical addition of mass was simulated via a Monte Carlo method that utilized the local photocarrier-generation rate to weight the local probabilities of mass. Thus, the computational results were principally defined by the fundamental light-matter interactions during deposition. Simulations similar to the experiments described in Figure 5.2 were performed, wherein two equal-intensity sources with $\lambda_{\text{avg}} = 630$ nm were utilized, with one source polarized vertically and the polarization of the second source offset clockwise from the vertical by θ_1 . However, unlike the experiment wherein incoherent sources were utilized, the simulations considered coherent sources. Simulations were performed for phase angles (ϕ) of either 0° or 90° between the two coherent sources. Figure 5.3(a)-(d) present simulations for $\theta_1 = 60^\circ, 70^\circ, 80^\circ,$ and 90° , respectively, for $\phi = 0^\circ$. The E-field vectors of the considered sources were identical to those plotted in Figure 5.2(a)-(d). In each case, a lamellar pattern was observed, and the orientation of the lamellar long axes displayed increasing rotations from the vertical with increasing values of θ_1 . Specifically, values of θ_{obs} of $33 \pm 3^\circ, 36 \pm 2^\circ, 40 \pm 2^\circ,$ and $45 \pm 1^\circ$ were measured for $\theta_1 = 60^\circ, 70^\circ, 80^\circ,$ and 90° , respectively. Figure 5.3(e) and (f)

present simulations analogous to those shown in Figure 5.3(a)-(d), but for a phase angle of $\phi = 90^\circ$. The E-field vectors of the sources were again identical to those presented in Figure 5.2(a)-(d). For $\theta_1 = 60^\circ$ (Figure 5.3(e)), the simulated morphology was lamellar and qualitatively similar to that observed with $\phi = 0^\circ$ (Figure 5.3(a)), whereas for $\theta_1 = 70^\circ$ (Figure 5.3(f)), the simulated morphology also displayed an oriented, lamellar-type component but appeared to be superimposed upon a mesh-type pattern. When $\theta_1 = 80^\circ$ (Figure 5.3(g)), the lamellar pattern was less well-defined and more similar in height to the mesh-type pattern, relative to the case of $\theta_1 = 70^\circ$. Moreover, when $\theta_1 = 90^\circ$ (Figure 5.3(h)), the morphology lacked any apparent anisotropy and orientation, and was thus similar to the morphology observed experimentally for growth stimulated by a single, unpolarized, incoherent source (Figure 5.1(d)).

The simulated morphologies displayed in Figure 5.3(a)-(d) showed that in the case of coherent sources with a phase difference of $\phi = 0^\circ$, only lamellar morphologies were observed. The sum of the output of two completely in-phase, coherent, linearly-polarized, same-wavelength sources cannot be differentiated from the output of a single coherent, linearly-polarized source that has an equivalent net intensity and the same polarization orientation as the weighted average polarization orientation of the tandem sources. Consequently, the photoelectrodeposit morphology observed for the case of a single incoherent source polarized at $\theta = 45^\circ$ (Figure 5.1(b)) was qualitatively matched by the simulated morphology for two equal intensity, in-phase ($\phi = 0^\circ$) coherent sources polarized at $\theta_0 = 0^\circ$ and $\theta_1 = 90^\circ$ (Figure 3(d)), with both exhibiting equivalent values of θ_{obs} . In addition, when $\phi = 0^\circ$, the

measured values of θ_{obs} was equivalent to the intensity-weighted average polarization orientation, $0.5 \cdot \theta_1$. In contrast, the sum of the output of two coherent, linearly-polarized, same-wavelength sources that are not completely in-phase ($\phi \neq 0^\circ$) can be differentiated from the output of a single coherent, linearly-polarized source with equivalent net intensity and the same polarization orientation as the weighted average polarization orientation of the tandem sources. In this case, the summing of the output of the tandem sources generates elliptically rather than linearly polarized illumination. The difference in the morphologies predicted by the simulations for growths with $\phi = 0^\circ$ and $\phi = 90^\circ$ suggests that the photoelectrodeposition process is capable of differentiating elliptically polarized from linearly polarized illumination. Hence, the resulting photoelectrodeposit physically encodes information concerning the relative phase of the illumination inputs.

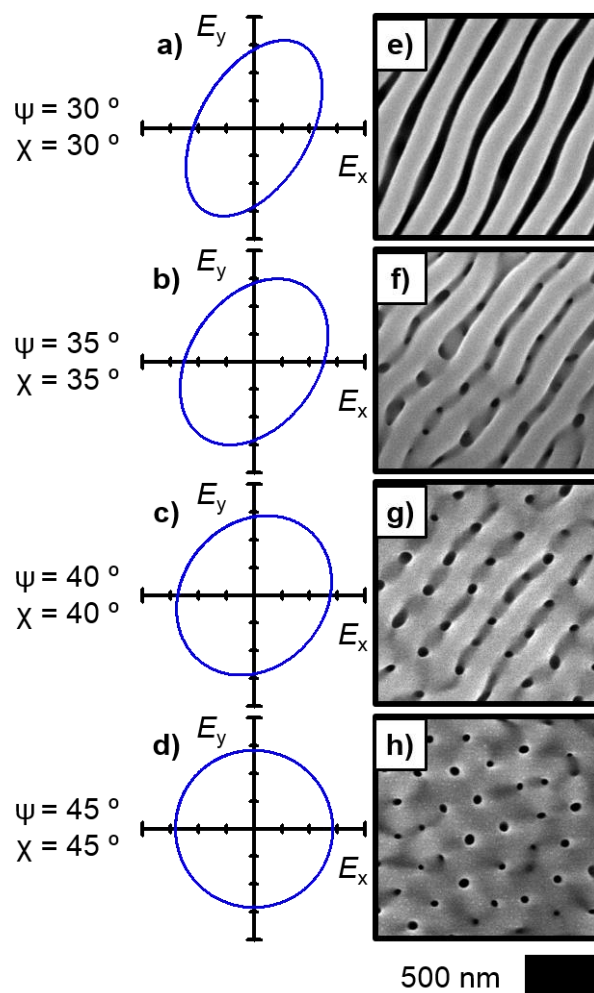


Figure 5.4. Effect of elliptical illumination polarization on photoelectrodeposit morphology. (a)-(d) Plots of the E-field vector traced over time at a fixed point for illumination provided by a HeNe laser $\lambda_{\text{avg}} = 632.8 \text{ nm}$ with defined elliptical polarizations. ψ indicates the orientation of the major axis of the ellipse measured clockwise from the vertical. χ represents the angle between the major axis and a line connecting a vertex on the major axis with one on the minor axis and relates the eccentricity and asymmetry of the ellipse. (e)-(h) SEMs representative of photoelectrodeposits generated with the elliptical illumination profiles indicated in (a)-(d), respectively.

Figure 5.4(a)-(d) presents plots of the polarization ellipses that result from the out-of-phase addition ($\phi = 90^\circ$) of sources with E-field vectors the same as those

plotted in Figure 5.2(a)-(d) and thus describe the illumination utilized in the simulations presented in Figure 5.3(e)-(h). The orientation of the major axis of the ellipse, measured clockwise from the vertical, is denoted as ψ . The angle between the major axis of the ellipse and a line connecting a vertex on the major axis with one on the minor axis, denoted as χ , quantifies the asymmetry, or eccentricity, of the ellipse. For the conditions investigated in the simulations presented in Figure 5.3(e)-(h), $\psi = \chi = 0.5 \cdot \theta_1$. Using these same elliptical polarizations, deposits were generated experimentally (with HeNe laser illumination with $\lambda_{\text{avg}} = 632.8 \text{ nm}$) to corroborate the conclusions from the simulations that the photoelectrochemical growth process can discriminate between linearly and elliptically polarized illumination, and thus responds to phase data contained in the incident illumination. The growth modeling indicated that this phenomenon manifests itself in the degree of nanoscale pattern anisotropy, and is potentially an effect of variable anisotropy in the illumination polarization. The addition of out-of-phase orthogonal polarization components results in the generation of an elliptical polarization state, and increasing amounts of such components decreases the asymmetry of the relevant polarization ellipse (quantified by χ). The simulations predict that as this asymmetry is reduced beyond a threshold ($\chi > 30^\circ$), the observable morphological patterning begins to transition from anisotropic to isotropic, and, in the limiting case of circular polarization ($\chi = 45^\circ$), the patterning becomes completely isotropic.

Figure 5.4(e)-(h) presents SEMs of the deposits that were generated utilizing the elliptical polarizations corresponding to those presented in Figure 5.4(a)-(d). Deposition with elliptical polarization with $\chi = 30^\circ$ (Figure 4(e)) resulted in the

generation of lamellar structures with highly uniaxial anisotropy, as in the case of linear polarization (Figure 1(b); $\chi = 0^\circ$ equivalent). For $\chi = 35^\circ$ (Figure 4(f)), the overall morphological anisotropy was reduced compared to the case for $\chi = 30^\circ$, and an isotropic mesh-type pattern was observed underlying the anisotropic lamellar pattern. For $\chi = 40^\circ$ (Figure 4(g)), this mesh-type morphology became more prominent, with a height approaching that of the anisotropic pattern. For $\chi = 45^\circ$ (Figure 5.4(h)), no anisotropic pattern was observed; rather, the morphology was highly similar to that produced by a single unpolarized incoherent source (Figure 5.1(d)). Thus, the experimental morphologies presented in Figure 5.4(e)-(h) matched those predicted by the growth model (Figure 5.3(e)-(h)). Such collective agreement demonstrates the capacity of the deposition to produce unique morphologies in response to elliptically polarized illumination, and thus to store relative phase information. Specifically, superimposed isotropic mesh-type patterns and anisotropic lamellar-type patterns are generated wherein the weighting between the two types of patterns is correlated with the phase difference between the orthogonal polarization components of the optical field (and thus the resultant ellipticity of the output).

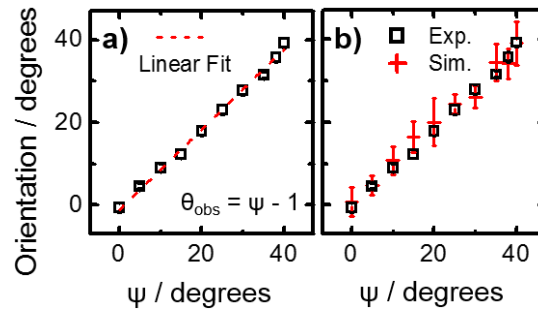


Figure 5.5. Orientation of photoelectrodeposit morphologies generated using elliptically polarized illumination derived from experimental results and computationally via growth modeling (a) Plot of the orientation of the pattern long axis (θ_{obs}) measured clockwise from the vertical as a function of ψ for photoelectrodeposits generated with elliptically polarized illumination. Error bars generally smaller than displayed symbols. (b) Same as (a) but with addition of values from growth modeling.

Auxiliary information regarding the polarization state of the incident illumination is also inherent in the lamellar-type pattern, because the pattern anisotropy is associated with an orientation. To characterize the relation between an elliptical polarization and the encoded orientation, additional deposits were generated experimentally using polarizations having $0^\circ \leq \psi \leq 25^\circ$ and $\chi = \psi$. Figure 5.5(a) presents values of θ_{obs} for $0^\circ \leq \psi \leq 40^\circ$ (wherein $\chi = \psi$) as a function of ψ . The trend is well-fit by a line of the form $\theta_{\text{obs}} = \psi - 1$. Additional growth modeling was performed to generate simulated morphologies for all of the experimentally investigated elliptical polarizations. Figure 5.5(b) plots the values of θ_{obs} derived from these simulations as a function of ψ , along with the corresponding experimental observations. Quantitative agreement was observed between the simulation and experiment. The near equivalence between θ_{obs} and ψ indicates that the directional component of the anisotropy of an elliptical polarization state is directly recorded in the deposit morphology. Moreover,

this anisotropy is discernible not only when the polarization is defined by a highly asymmetric ellipse (small values of χ , approximating linear polarization) but also when the polarization is defined by a near-circular ellipse, e.g. $\chi = 40^\circ$ (Figure 5.4(h)). This behavior indicates that when the illumination used in the deposition process is supplied by tandem sources, the lamellar component of the morphology arises from the in-phase addition of orthogonal polarization components, whereas the mesh component arises from out-of-phase addition. This behavior and rationale is consistent with the observations of the morphologies generated using two near-orthogonal or orthogonal equal intensity incoherent sources (Figure 5.2). As observed for the analogous simulations (Figure 5.3(e)-(h)) and experiments (Figure 5.4(e)-(h)) with coherent sources with $\phi = 90^\circ$, only a lamellar-type morphology was observed for $\theta_1 = 60^\circ$ ($\theta_0 = 0^\circ$) whereas a lamellar-type morphology superimposed on a mesh-type was observed for $\theta_1 = 70^\circ$ and 80° . In each case, the lamellar morphology was oriented along the intensity-weighted average polarization orientation. However, in contrast to deposits generated using coherent sources with $\phi = 90^\circ$, the lamellar morphologies were more prominent for $\theta_1 = 70^\circ$ and 80° , and for $\theta_1 = 90^\circ$, some anisotropy was still observed. This behavior results from the presence of in-phase addition in complement to the out-of-phase addition solely present in the coherent case with $\phi = 90^\circ$, as the summing of the incoherent sources involves many additions with a continuous range of phase angles ($0^\circ \leq \phi \leq 90^\circ$), in contrast to the coherent case for which ϕ was fixed at 90° . Similarly, the absence of a discernible mesh-type morphological component in the incoherent case with $\theta_1 = 60^\circ$ is consistent with an insufficient amount of out-of-phase addition of orthogonal polarization components.

5.3 Conclusions

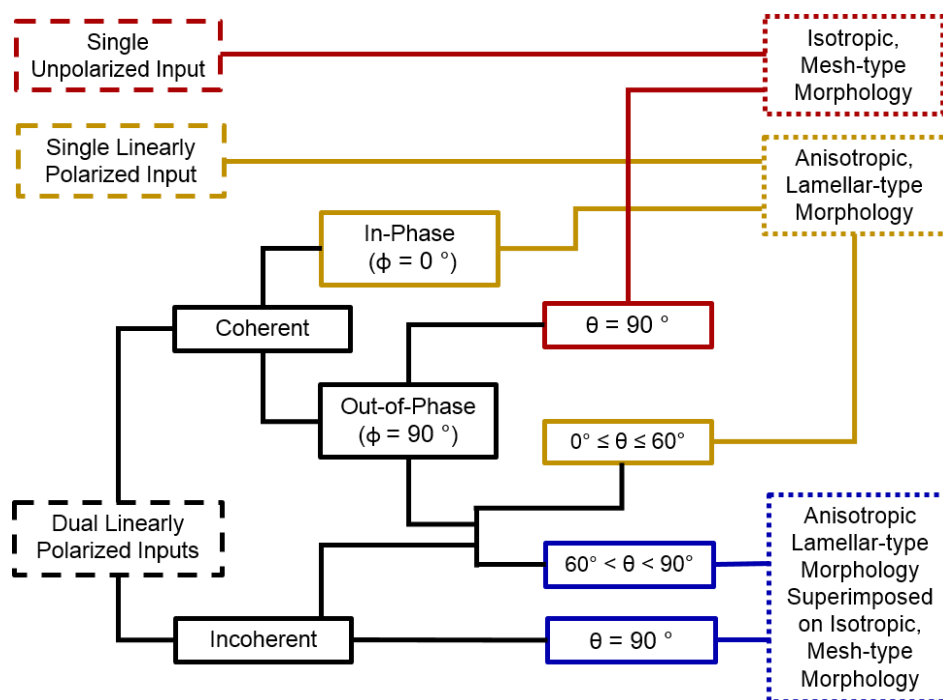


Figure 5.6. Flowchart detailing expected photoelectrodeposit morphology as a function of the polarization characteristics of the optical inputs. θ represents the angle between the polarization vectors of two linearly polarized inputs and ϕ represents the phase angle between two coherent inputs. Simultaneous inputs are assumed to be of equal intensity. Anisotropic morphologies orient with long axes parallel to the average polarization vector of the input(s).

Figure 5.6 presents a flowchart that outlines the morphology of the photoelectrodeposit as a function of the polarization characteristics of the optical inputs. In summary, photoelectrodeposition using a single, linearly polarized source resulted in the generation of a highly anisotropic, lamellar-type morphology, whereas the use of an unpolarized source resulted in the generation of an isotropic, mesh-type morphology. The use of tandem simultaneous same-wavelength, linearly polarized,

coherent and in-phase sources also resulted in the generation of lamellar-type structures, because such illumination is equivalent to that produced by a single linearly-polarized coherent source. Summing two linearly polarized, coherent sources that are not completely in-phase results in elliptically polarized illumination. The use of such illumination generated a spectrum of related morphologies that were dependent on the ellipticity, which correlates with the amount of out-of-phase addition between orthogonally polarized components of the optical inputs. For sufficiently low degrees of ellipticity ($\chi \leq 30^\circ$), lamellar morphologies that appear equivalent to those generated using a single linearly polarized source were observed. For greater degrees of ellipticity, lamellar-type patterns were superimposed on a mesh-type pattern that was similar to the pattern observed when unpolarized illumination was used. Relative to the lamellar-type pattern, the mesh-type pattern increased in height and definition as the degree of the polarization ellipticity increased. Only the mesh-type pattern was observed in the limiting case of circular polarization ($\chi = 45^\circ$). The results of deposition using two linearly polarized, incoherent sources were consistent with those observed for the use of two coherent sources that were not completely in-phase, in that anisotropic, lamellar-type morphologies transitioned to isotropic, mesh-type morphologies as the amount of out-of-phase addition increased between the orthogonally polarized components of the light sources. When tandem sources were used and lamellar-type morphologies were generated, the long axis of the lamellar pattern always aligned parallel to the intensity-weighted average polarization orientation. The observed morphologies consistently matched those simulated by computational modeling, indicating that the specific morphology was fully determined by each set of defined

optical inputs. Thus, the collective experimental and computational modeling data indicate that the photoelectrochemical growth process is sensitive to the coherency, relative phase, and polarization orientations of the utilized illumination inputs, and that the resulting morphology expresses these inputs in a distinctive pattern in each case.